[American Journal of Science, Vol. 316, December, 2016, P. 1027-1053, DOI 10.2475/10.2016.03]

THE EFFECT OF SOLUTION CHEMISTRY ON NUCLEATION OF NESQUEHONITE

CHEN ZHU*,§, ZHENGRONG WANG**,§,†, and LIANG ZHAO*,†

ABSTRACT. Several series of nesquehonite nucleation experiments (62 experiments in total) were conducted in aqueous solutions having Mg^{2+}/CO_3^{2-} activity ratios (here referring to $log(a_{Mg^{2+}}/a_{CO_3^{2-}})$) ranging between −0.96 to 2.89, but different saturation states (Ω ranging between 2.49–6.90) and solution pH. The goal was to understand the effect of solution chemistry on the nucleation of nesquehonite. Our experimental results show that induction-time estimates from our precipitation experiments with similar Mg^{2+}/CO_3^{2-} activity ratios are consistent with classical nucleation theory (CNT), while the surface energy derived from CNT varies with Mg^{2+}/CO_3^{2-} activity ratios. The induction times of nesquehonite nucleation are scattered noticeably when the saturation state of solution is low (Ω < 4), and the nuclei surface energy, derived from the relationship between induction time and saturation state of solution, increases with increasing Mg^{2+}/CO_3^{2-} activity ratios. These observations can be explained by the different absorption behaviors of Mg^{2+} and CO_3^{2-} and/or reduced Gibbs free energies through better screening of the electric double layer. A surface energy model involving solution composition is developed that combines surface complexation with electrostatic models. This new model takes into account how surface charge may affect surface energy. This model implies that the highest surface energy may occur around the point of zero charge (p.z.c), where the nucleation is fastest (or conversely, where the induction time is shortest) under low saturation states, but not under high saturation states. An accelerated attachment kinetic of monomers is also expected at the p.z.c. where high energy surface requires surface absorbed ions to have higher reactivity. This study provides deeper insight into mechanisms of nesquehonite nucleation in nature, and guidelines for accelerating the precipitation rates of nesquehonite.

Keywords: Nucleation, surface energy, absorption, surface charge, induction-time

INTRODUCTION

Background

The studies of nucleation and precipitation kinetics of nesquehonite have recently attracted much attention, partly because nesquehonite is a natural weathering product of Mg-rich mafic/ultramafic rocks, but also because nesquehonite is a promising medium for anthropogenic CO_2 sequestration since it precipitates rapidly at ambient temperatures (for example O'Connor and others, 2005; Ferrini and others, 2009; Zhao and others, 2013). Significant efforts have been made to accelerate its nucleation rate in solutions, and a better understanding of nucleation processes can help. For example, it has been shown that the strong solvation of Mg-ions in aqueous solution limits the rate of magnesium-carbonate nucleation (for example Sayles and Fyfe, 1973), but the energy barrier can be overcome partly by promoting kinetic aggregation through the addition of organic solvent (Zhao and others, 2013).

Nesquehonite is a kinetically favored precipitate from aqueous solutions at temperatures below 52 °C (for example Davies and Bubela, 1973). However, hydromag-

* Key Laboratory of Surficial Geochemistry, Ministry of Education, School of Earth Sciences and Engineering, Nanjing University, Nanjing 210093, P.R. China
§ Department of Geology and Geophysics, Yale University, P.O. Box 208109, New Haven, Connecticut 06520, USA
** Department of Earth & Atmospheric Sciences, City College of New York, CUNY, New York, New York 10031, USA
† Corresponding authors: zwang1@ccny.cuny.edu; zhaoliang@nju.edu.cn; zhuchen.nju@gmail.com

nesite ($Mg_5(CO_3)_4(OH)_2{\cdot}xH_2O$, where x is the number of crystalline waters in a unit cell) and magnesite ($MgCO_3$) are, in fact, the most abundant magnesium-carbonate minerals found in nature. In contrast, nesquehonite ($MgCO_3{\cdot}3H_2O$) is rarely found (for example Fischbeck and Müller, 1971; Jull and others, 1988; Power and others, 2007) because it is metastable relative to magnesite under Earth's surface conditions, and nesquehonite slowly transforms into hydromagnesite through dissolution/reprecipitation and CO_2 degassing (for example Dong and others, 2008; Hopkinson and others, 2008). A previous study using advanced *in situ* total-reflection Fourier-transform infrared (ATR-FTIR) and Raman spectroscopy confirmed the transformation of nesquehonite to hydromagnesite in solution. The spectroscopy also suggested that the saturation state of solution with respect to nesquehonite controls the precipitation kinetics at ambient temperatures (Hänchen and others, 2008). Thus, nesquehonite could act as a precursor of natural hydromagnesite or magnesite. Surface energy may play an important role during these precipitation and transformation processes since mineral phases with lower surface energy (nesquehonite) tend to precipitate prior to the thermodynamically more stable phases (magnesite) regardless of the actual nucleation paths (for example De Yoreo and others, 2015).

The interfaces between minerals and aqueous solutions are key places where important Earth surface processes occur, including chemical weathering, mineral dissolution/precipitation, and pollutant absorption/release (for example Langmuir, 1916). Mineral surface properties, such as the surface structure and the surface energy, determine the outcomes of many geochemical reactions. In particular, surface energy of mineral is essential to determining when and where crystals start to precipitate, and the solubility of crystals of different sizes (for example in the Ostwald–Freundlich equation). The surface energy originates from dangling chemical bonds at the solid-liquid interface. In some cases, the excess surface energy from these bonds could be so significant that it can even reverse the stability sequence of polymorphs (for example De Yoreo and others, 2015). Several factors could affect surface energy, but the effect of solution chemistry, particularly the solution stoichiometry, on the surface energy and nucleation process is poorly understood.

This study aims to investigate the effect of solution chemistry on the nucleation of nesquehonite. To achieve this goal, dozens (62) of nucleation experiments were carried out to precipitate nesquehonite out of solutions at similar Mg^{2+}/CO_3^{2-} activity ratios, but at different saturation states and solution pHs. As we discuss below, our results show that nucleation rate is a function of both saturation state and solution stoichiometry. These observations can be explained by significant changes in surface energy caused by either selective absorption of ions and/or surface charging of the nuclei themselves. This study provides an experimental and theoretical framework for a better understanding of the nucleation of minerals from aqueous solution.

Notations	
a	Shape factor of nuclei
a_i	Activity of species i
A	Surface area
D	Dielectric constant of water, 78.5 at 298K
E_A	Energy barrier for monomer attachment
e	Elementary electric charge, 1.602×10^{-19}, C
F	Faraday constant, 96485.33, C/mol
G	Gibbs free energy
G_s	Gibbs free energy of surface space
$G(n)$	Gibbs free energy of nuclei with size n
h	Planck constant, $6.62606957 \times 10^{-34}$, J•s
I	Ionic strength
ΔI_i	Intensity differences between two light beams

Notations	
IAP	Ionic product
J	Nucleation rate
K_i	Intrinsic stability constant of surface reaction i
K_{sp}	Solubility product
k_B	Boltzmann constant, $1.380\,6488 \times 10^{-23}$, J/K
ln	Napierian logarithms
log	logarithms in base 10
N_A	Avogadro constant, 6.022141×10^{23}, mol^{-1}
N_{det}	Number detection limit of induction time measurement method
N_v	Number of monomers per unit volume of the nuclei, m^{-3}
N^*	Number of monomers near the critical nuclei
n	Number of monomers or species
$n_+^\ddagger$	Number of monomers in critical nuclei
R	Ideal gas constant, 8.3144621, J/(K•mol)
r	Distance from origin point in spherical coordinates
r_0	Radius of spherical particle
T	Temperature, K
t_{ind}	Nucleation induction time, s
V	Volume of crystallization system
x	Distance to charged surface
z_i	Valence of surface species i
Γ_i	Surface density of absorbate, mol/m^2
γ	Surface energy of nuclei, mJ/m^2
γ_0	Structural surface energy, mJ/m^2
ε_0	Vacuum permittivity, $8.854187817620 \times 10^{-12}$, C/(V•m)
μ	Chemical potential
σ	Charge density, C/m^2
σ_0	Surface charge density, C/m^2
ν	Fundamental frequency, $v = k_BT/h$, s^{-1}
ν_0	Volume per molecule in nesquehonite, 1.249×10^{-28} m^3
Ψ	Electrical potential, V
Ψ_0	Electrical potential on particle surface, V
Ω	Saturation state of nesquehonite
κ	Debye length

Theoretical

Extracting surface energies from induction time measurements.—Classical nucleation theory (CNT) assumes that the surface free energy presents as an energy barrier prohibiting the nucleation of mineral droplets (for example Mullin, 2001). It was initially developed to describe the condensation of vapors, however, and only later applied to the precipitation of mineral phases. Control by saturation state (Ω) of nucleation rates is central to CNT (for example Mullin, 2001), however, no previous studies have been designed to examine if solution stoichiometry, at a constant saturation state, could also affect nucleation rates.

The CNT separates the energy responsible for nucleation into two terms: the surface free energy gain (which is unfavorable for precipitation) and bulk free energy loss (which is favorable for precipitation) due to nucleus enlargement (for example Mullin, 2001). Equation (1) describes the Gibbs free energy (G) in the system that precipitates crystal nucleus (for example Wu, 1996):

$$G(n) = -n\Delta\mu + a\gamma n^{\frac{2}{3}} \tag{1}$$

where n is number of monomers in a nucleus, $\Delta\mu$ is chemical potential difference between metastable and stable phases which often relates to $k_BTln(\Omega)$ (k_B is Boltzmann constant, T is absolute temperature), a is shape factor, from which the surface area of a nucleus can be calculated, that is, $a = 4.84v_0^{2/3}$ for sphere, $a = 6v_0^{2/3}$ for cube, $a = 7.21v_0^{2/3}$ for

tetrahedron, and a = $5.72v_0^{2/3}$ for octahedron (v_0 is volume per monomer in stable phase), and γ is excess Gibbs energy per surface area of nucleus compared to the bulk phase, which may vary with mineral phases. The theory also assumes that a monomer is the smallest building block for crystal growth (for example one $MgCO_3 \cdot 3H_2O$ unit in this study).

The CNT also assumes the presence of a critical nucleus size, $n^{\ddagger}$ (the critical number of monomers in a nucleus), at the top of the energy barrier (that is when $\partial G/\partial n = 0$). Using this constraint in equation (1) leads to equation (2):

$$n^{\ddagger} = \left(\frac{2\gamma a}{3\Delta\mu}\right)^3 \tag{2}$$

When Gibbs free energy $G(n^{\ddagger})$ reaches a maximum, it may be expressed as:

$$G(n^{\ddagger}) = \frac{4(\gamma a)^3}{27\Delta\mu^2} \tag{3}$$

Assuming the number of critical nuclei per unit volume follows a Boltzmann distribution law (for example White, 2013), $n_{critical}=N_v \exp(-G(n^{\ddagger})/k_BT)$, the nucleation rate *J*, the number of nuclei formed per unit time per unit volume, can be expressed as the attachment frequency (A) times the number of critical nuclei ($n_{critical}$):

$$\begin{aligned} J &= AN_v \exp\left(\frac{-G(n^{\ddagger})}{k_BT}\right) \\ &= AN_v \exp\left(\frac{-4(\gamma a)^3}{27(k_BT)^3(\ln(\Omega))^2}\right) \end{aligned} \tag{4}$$

where N_v is number of monomers per unit volume of nuclei. The attachment frequency (A) in equation (4) can be expressed as follows (White, 2013):

$$A = N^* v \exp\left(\frac{-E_A}{k_BT}\right) \tag{5}$$

where N^* is the number of monomers near the critical nuclei; $v = k_BT/h$ is the fundamental frequency. This equation describes the attachment frequency of monomers to the critical nuclei, which is the multiplication product of the number of monomers adjacent to the cluster (N^*), the number of attaching attempts (v), and the probability of attachment success ($\exp(-E_A/k_BT)$) as a function of energy barrier (E_A) for monomer attachment and temperature (T).

The CNT typically assumes that induction time is inversely proportional to nucleation rate (for example Kashchiev and van Rosmalen, 2003; Kubota and others, 2014):

$$t_{ind} = \frac{1}{JV} \tag{6a}$$

where *V* is the volume of the crystallization system. Equation (6a) is useful experimentally if a detection system could identify crystals as they initially precipitate, regardless of size. Because detection schemes are never perfect, the practical induction time always includes a detection limit, or lag time, as expressed in equation (6b) as follows:

$$t_{ind} = \frac{N_{det}}{JV} \tag{6b}$$

where N_{det} is detection sensitivity of a specific method. Although different detection methods may lead to different induction times (t_{ind} and *J*) even if experiments are

conducted under identical conditions, they will not affect the calculated surface energies if such methods are based on measuring the number density of nuclei in solution (for example Kubota and others, 2014). Combining equation (6b) with equations (4) and (5) yields the following equation:

$$\ln(t_{ind}) = \frac{B\gamma^3}{T^3(\ln\Omega)^2} + \frac{E_A}{k_B T} - \ln\left(VN^*\upsilon\frac{N_v}{N_{\text{det}}}\right) \tag{7}$$

where $B = 4a^3/27k_B^3$. This equation implies that, at a given temperature, a plot of $\ln(t_{ind})$ versus $(\ln(\Omega))^{-2}$ yields a straight line. The slope of this line allows estimate of surface-energy differences among crystals, their substrates, and solution at a given temperature and nucleus geometry. The slope would, for example, allow estimates of surface-energy differences between crystals and solution for homogeneous nucleation. The intercept of the data relates to detection sensitivity and other kinetic parameters. Note that equation (7) explicitly implies that the surface energy derived from induction time shall not be affected by detection sensitivity (that is N_{det}). This independence is important.

Thermodynamics of surface energy.—The surface energy can affect not only the induction time, but also the thermodynamic properties of nesquehonite during nucleation. If *G* is the Gibbs free energy of system, γ can be defined as follows (Parks, 1990):

$$\gamma = \left(\frac{\partial G}{\partial A}\right)_{P,T,n} \tag{8}$$

In a system containing multiple chemical species and surfaces, the total free energy change can be written as follows:

$$dG = -SdT + VdP + \sum_i \mu_i dn_i + \sum_j \gamma_j dA_j \tag{9}$$

Under constant pressure and temperature, the free energy change in equation (9) can be simplified as follows:

$$dG = \sum_i \mu_i dn_i + \sum_j \gamma_j dA_j \tag{10}$$

Then, the Gibbs energy change of a specific interface surface can be written as follows:

$$dG_s = \sum_i \mu_{s,i} dn_{s,i} + \gamma dA \tag{11}$$

The change of total Gibbs energy (including surface energy) consists of changes in surface area and surface species at a given temperature. For charged species that are absorbed on a charged surface, the chemical potential ($\tilde{\mu}_i$) should also include the electrical potential energy of ions in the electrical field (Lyklema, 1991), which can be written as follows:

$$\tilde{\mu}_i = \mu_i + z_i F\Psi \tag{12}$$

where z_i is valence of species that could be found on mineral surfaces, *F* is Faraday constant and Ψ is electric potential. When ions in solution are attracted to counter-charges on mineral surfaces, dielectric screening reduces the electric potential of species on mineral surfaces (Lyklema, 1991). The Gibbs energy of electrical double layer can be expressed as the integral of $\int_0^{\Psi_0}\sigma d\Psi$, where σ is charge density at a position

away from the interface, and Ψ is electric potential, which also varies with distance. Thus, the Gibbs energy of the interface can be written as follows:

$$G_s = \gamma A + \sum_i \mu_i n_{s,i} + \int_0^{\Psi_0} \sigma A d\Psi \tag{13}$$

The total derivative is:

$$dG_{s,tot} = \gamma dA + A d\gamma + \sum_i \mu_i dn_{s,i} + \sum_i n_{s,i} d\mu_i + \sigma A d\Psi \tag{14}$$

Since Gibbs free energy is a state function, equations (11) and (14) can be considered equal ($dG_{s,tot} = dG_s$). The change of surface energy can then be written as:

$$d\gamma = -\sum_i \frac{n_{s,i}}{A} d\mu_i - \sigma d\Psi = -\sum_i \Gamma_i d\mu_i - \sigma d\Psi \tag{15}$$

Equation (15) states that surface energy consists of two terms. The first term is the classical Gibbs adsorption isotherm (for example Hunter, 2001), which implies that any positive absorption (that is the concentration of an absorbate on nuclei surface correlates positively with its concentration in solution) reduces surface energy. The second term describes the work needed to move a charged ion that is at a position near the charged surface to infinity. Work decreases as a counterion approaches the charged surface (for example the formation of electric double layer) and increases for a co-ion. The effect of the second term has also been experimentally verified. For example, measurements of polytetrafluoroethylene (PTFE) surface energy under various sodium chloride concentrations have shown that the electrostatic forces can also change the surface energy even when no absorption occurs (for example Butkus and Grasso, 1998). The material-specific surface energy γ_0 (which is determined by the composition of solid when there is no absorption of ions on solid surface) can be described as follows (Mersmann, 1990):

$$\gamma_0 = 0.414 k_B T \frac{1}{\sqrt[3]{v_0^2}} \ln\left(\frac{\rho}{M\sqrt{K_{sp}}}\right) \tag{16}$$

where k_B is Boltzmann constant; T is absolute temperature in Kelvin; ν_0 is volume of a mineral monomer; M, ρ and K_{sp} represent the molar mass, density and solubility product of a mineral phase, respectively. For nesquehonite, its material-specific surface energy calculated by equation (16) is 58.1 mJ/m^2 at 298K, using the solubility product $K_{sp} = 10^{-5.16}$ (Zhao and others, 2013). Note that γ_0 should be considered as the energy of a mineral surface when affected only by hydration, rather than in a vacuum, since γ_0 is calculated from nucleation in solution. It is worth noting that, although widely applied to aqueous phase crystallization, surface energy values determined in disparate experiments can be inconsistent in various studies because of discrepancies in experimental conditions besides temperature, pressure and starting materials. Although the idea that interfacial energy varies with surface charge (or other adsorbate concentration) is widely recognized (for example Butkus and Grasso, 1998; Giuffre and others, 2013), no systematic study exists.

Based on equation (15), the surface energy in electrolyte solution can be defined as follows:

$$\gamma = \gamma_0 - RT\sum_i \Gamma_i - \int_0^{\Psi_0} \sigma(\Psi) d\Psi \tag{17}$$

The second term in equation (17) ($-RT\sum_i \Gamma_i$) is the classical Gibbs absorption isotherm. Its formulation implies that any positive absorption reduces the surface energy and *vice versa*. Moreover, the last term in equation (17) indicates that the relationship between surface charge density σ and surface electric potential Ψ is the key.

Factors affecting surface charge and surface potential.—The surface charge (σ_0) and surface potential (Ψ_0) together determine the electrical contribution to Gibbs energy on a mineral surface. The ionic strength of solution evidently affects the surface potential because they control the length of electric double layer. Mineral geometry also plays important roles on modifying surface charge and electric potential. Different shapes result in different gradients of electric field in space. For a flat surface, the Poisson equation relating potential and space charge density may be written as follows:

$$\nabla^2\Psi(x) = \frac{d^2\Psi(x)}{dx^2} = -\frac{\rho(x)}{\varepsilon_0 D} \tag{18}$$

where ε_0 is permittivity in vacuum, D is dielectric constant of solution, and x is distance from the flat surface. The space charge density $\rho(x)$ in turn relates to local electrolyte concentrations as:

$$\rho(x) = F\sum_j z_j c_j(x) \tag{19}$$

Assuming counterions are volumeless and that a diffuse layer exists next to the surface of solid, a simplified equation that relates the charge density to the electric potential can be written:

$$\sigma = \sqrt{8\varepsilon_0 DRTI}\, sinh\left(\frac{F\Psi}{2RT}\right) \tag{20}$$

In spherical coordinates, the Poisson equation can be written:

$$\frac{1}{r^2}\frac{d}{dr}\left(r^2\frac{d\Psi}{dr}\right) = \left(\frac{d}{dr} + \frac{2}{r}\right)\frac{d\Psi}{dr} = -\frac{\rho(r)}{\varepsilon_0 D} \tag{21}$$

where x is replaced by r, the radial distance in spherical coordinates. After adopting the Debye length, κ^{-1}, the relationship between charge density and electric potential can be expressed in two different equations depending on the product of κx_0.

For large κx_0:

$$\sigma_0 = \varepsilon_0 D_\kappa \Psi_0 \text{ (denoted as the 'SDL-1' model in subsequent discussion)} \tag{22}$$

and for small κr_0:

$$\sigma_0 = \frac{\varepsilon_0 D\Psi_0}{2\kappa r_0} \text{ (denoted as the 'SDL-2' model)} \tag{23}$$

where r_0 represents the radius of the spherical surface (Lyklema and others, 1995). In solutions of high ionic strength, the increased concentration of ions effectively shields the charged surface and decrease the Debye length and the surface potentials.

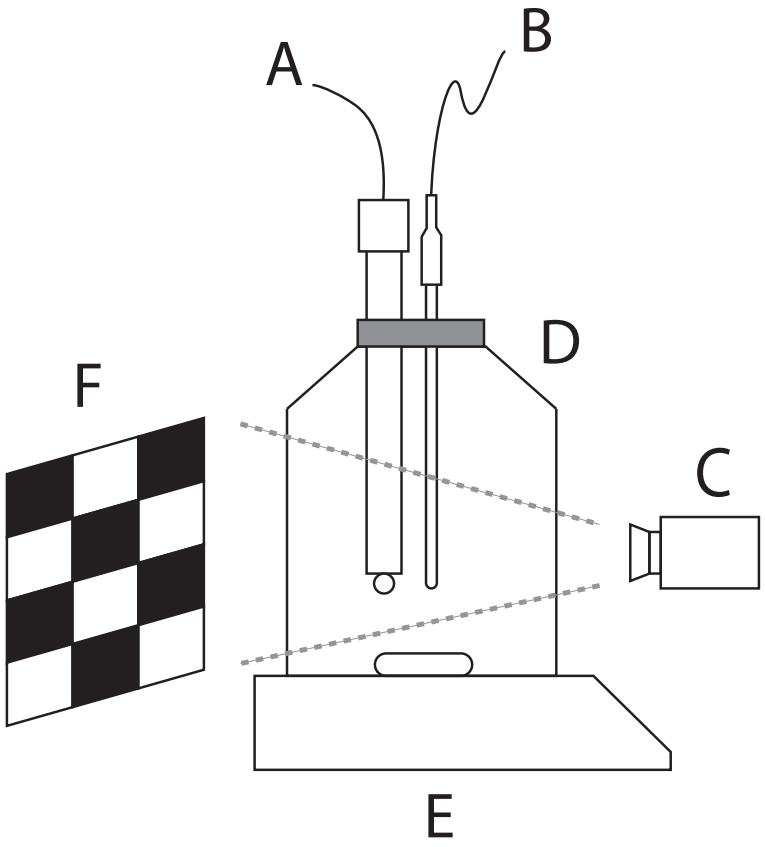

Fig. 1. Experimental set-up for precipitating nesquehonite: (A) pH electrode, (B) temperature probe, (C) digital camera, (D) Corning® polystyrene storage bottle, (E) magnetic stirrer, and (F) checkered background plate.

These theoretical considerations clearly imply that the surface energy of a particle in solution is controlled by processes that include the absorption ions and electric interactions, all of which may also affect the nucleation of crystals.

EXPERIMENTS

Materials and Experimental Procedure

A batch (2 kg) of 0.9995 mol/kg $MgCl_2$ stock solution was first made by dissolving analytical grade reagent $MgCl_2 \cdot 6H_2O$ (J.T.Baker®, Avantor Performance Materials, Inc.). A preset amount of this Mg stock solution was then mixed with water to make a diluted solution for experiments (denoted as 'Solution A'). Another solution (denoted as 'Solution B') was made by dissolving a certain quantity of analytical grade $NaHCO_3$ (Sigma-Aldrich®) in 18 MΩ water to serve as a carbonate stock solution. The $NaHCO_3$ and NaOH solids were dissolved together in such a way as to minimize CO_2 degassing. Both solution A and B were filtered by ~0.22 μm membrane and placed in a ~25 °C water bath before mixing.

When the temperatures of both solutions were stable, solution B was brought out of the water bath and placed on a magnetic stirrer operating at ~300 rpm (fig. 1).

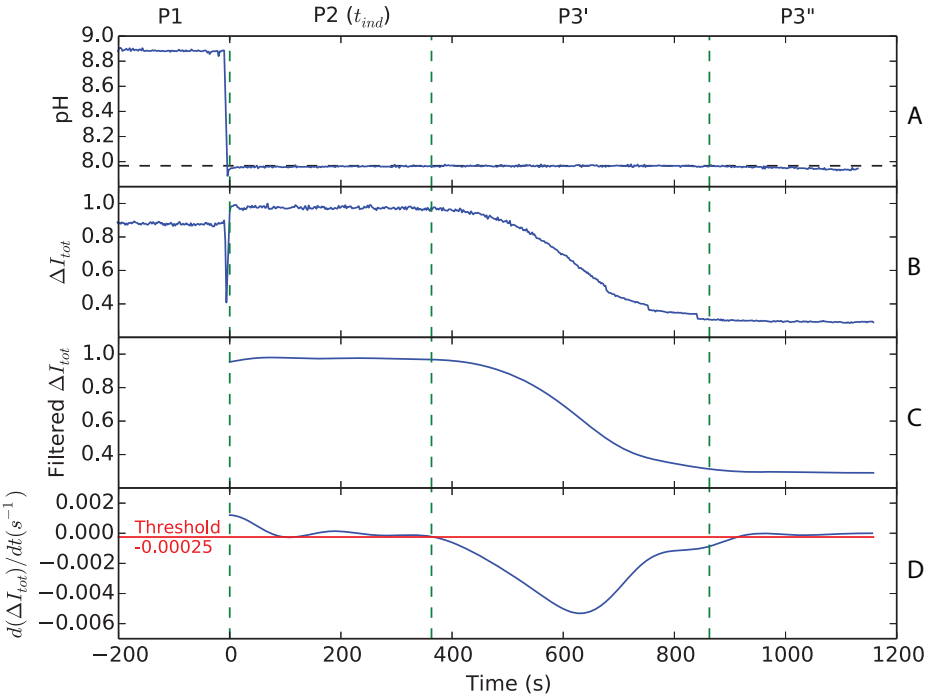

Fig. 2. The variation of pH values and total light intensity contrast as a function of time in our precipitation experiment D51 (as an example): (A) solution pH measurement; (B) unsmoothed total light intensity difference(ΔI_{tot}); (C) short-noise-filtered total-light-intensity difference (ΔI_{tot}); and (D) the first derivative of ΔI_{tot}. A threshold for the first derivation of ΔI_{tot} was applied to mark the change in solution transparency/turbidity. P1 through P3 represent different crystallization periods and the nucleation induction time is defined as the duration of P2.

Solution A was then poured into the bottle containing solution B within 5 seconds, which was then sealed. A pH electrode (with a sensitivity of 0.001) and a thermocouple were placed in the solution through sealed holes and the pH value and temperature of solution were continuously recorded. The achievement of homogeneous mixture was determined as the onset of a stable pH value (P2 in fig. 2). A digital camera was in place to constantly take pictures of the solution with a frequency of 30 pictures/second (fig. 1) through the container. Experiments were stopped when the solution lost transparency. Pictures taken by the camera were then processed to estimate the induction time (see *Determination of Induction time* in the next section). A new pair of solution A and B were made for experiments that have a different saturation state and a different Mg^{2+}/CO_3^{2-} activity ratio. A new polystyrene container was also used in each experiment to ensure the absence of crystal seeds and to ensure that nucleation was homogeneous (see Appendix I).

Continuous monitoring of experimental temperature showed a small fluctuation in our experiments (24.1-25.2 °C, as listed in table 1). However, the typical temperature variation of a single experiment life cycle was ≤0.1 °C for the first hour, which is longer than most of the induction-time estimates compiled in table 1 and thus the temperature fluctuations, which are small, do not affect our conclusions.

An aliquot of solid samples was collected after the induction period when solution transparency was constant (~2 hours after initial mixing). The mineralogy was characterized by X-ray Diffraction (XRD; Bruker D8 Focus Powder X-ray Diffractom-

Table 1

Solution chemistries and induction times measured in nesquehonite crystallization experiments

ID	T	Total Mg	Total Cl	Total C (DIC)	Total Na	pH	Ω	$log\left(\frac{a_{Mg^{2+}}}{a_{CO_3^{2-}}}\right)$	I	t_{ind}
#	°C	*mol/kgs*	*mol/kgs*	*mol/kgs*	*mol/kgs*				*mol/kgs*	*s*
1	24.4	0.0308	0.0617	0.2023	0.3590	9.73	3.23	-0.96	0.47	514
2	24.6	0.0308	0.0617	0.2023	0.3604	9.73	3.22	-0.96	0.47	521
A3	25.0	0.0500	0.1000	0.2023	0.3177	9.67	5.10	-0.60	0.47	210
A4	24.9	0.0500	0.0999	0.2023	0.3173	9.64	5.07	-0.57	0.46	242
A5	25.0	0.0438	0.0876	0.2026	0.3144	9.62	4.45	-0.64	0.45	218
A6	25.0	0.0438	0.0876	0.2030	0.3133	9.57	4.40	-0.60	0.44	217
A7	25.0	0.0369	0.0737	0.2025	0.3034	9.54	3.72	-0.66	0.42	337
A8	25.1	0.0369	0.0738	0.2029	0.2980	9.49	3.67	-0.60	0.41	308
A9	25.0	0.0300	0.0600	0.2023	0.2772	9.40	2.93	-0.62	0.38	422
A10	25.0	0.0300	0.0599	0.2023	0.2774	9.39	2.92	-0.60	0.37	479
11	24.9	0.0370	0.0739	0.2026	0.2886	9.39	3.54	-0.48	0.39	269
12	24.8	0.0369	0.0738	0.2028	0.2704	9.21	3.26	-0.28	0.37	292
13	25.2	0.0319	0.0637	0.2024	0.2698	9.28	2.95	-0.46	0.36	370
14	25.0	0.0321	0.0641	0.2025	0.2556	9.14	2.73	-0.26	0.34	652
B15	25.0	0.0647	0.1294	0.2029	0.3038	9.43	5.97	-0.19	0.46	121
B16	24.9	0.0539	0.1078	0.2024	0.2769	9.18	4.49	-0.02	0.40	284
B17	25.0	0.0460	0.0920	0.2022	0.2765	9.23	4.00	-0.17	0.39	270
B18	24.9	0.0460	0.0920	0.2023	0.2738	9.20	3.95	-0.14	0.39	290
B19	25.1	0.0460	0.0919	0.2022	0.2712	9.16	3.85	-0.10	0.38	297
B20	24.9	0.0398	0.0796	0.2024	0.2907	9.10	3.19	-0.09	0.38	346
B21	24.9	0.0382	0.0765	0.2007	0.2428	9.05	3.04	-0.05	0.34	522
B22	25.0	0.0321	0.0642	0.2025	0.2557	9.13	2.73	-0.26	0.34	852
B23	25.0	0.0321	0.0642	0.2024	0.2556	9.13	2.72	-0.25	0.34	660
B24	25.0	0.0321	0.0642	0.2024	0.2556	9.13	2.72	-0.25	0.34	660
B25	25.0	0.0321	0.0642	0.2024	0.2554	9.12	2.71	-0.24	0.34	623
B26	25.0	0.0321	0.0641	0.2024	0.2555	9.12	2.71	-0.24	0.34	767
B27	25.0	0.0321	0.0641	0.2025	0.2556	9.12	2.70	-0.24	0.34	689
B28	25.0	0.0319	0.0639	0.2024	0.2555	9.08	2.62	-0.19	0.34	699
29	25.0	0.0539	0.1077	0.2019	0.2688	9.09	4.20	0.09	0.40	247
30	24.9	0.0460	0.0920	0.2022	0.2702	8.96	3.27	0.16	0.37	261
31	25.1	0.0499	1.1485	0.2022	1.3388	9.04	3.18	0.43	1.62	274
32	25.0	0.0499	1.1488	0.2023	1.3392	9.04	3.16	0.44	1.62	243
33	24.8	0.0398	0.0796	0.2024	0.2752	8.97	2.88	0.08	0.36	391
34	25.1	0.0400	0.0800	0.2024	0.2523	8.81	2.49	0.30	0.35	732
C35	24.9	0.1234	0.2467	0.2047	0.2719	8.87	6.90	0.86	0.57	127
C36	24.7	0.1235	0.2471	0.2023	0.2635	8.82	6.50	0.92	0.57	149
C37	24.8	0.1236	0.2471	0.2023	0.2643	8.79	6.33	0.95	0.57	166
C38	24.9	0.0985	0.1970	0.2037	0.2633	8.77	5.18	0.83	0.50	202
C39	25.0	0.0985	0.1971	0.2035	0.2584	8.72	4.90	0.88	0.50	213
C40	24.9	0.0986	0.1971	0.2036	0.2525	8.62	4.34	0.99	0.50	219
C41	24.5	0.0846	0.1693	0.2030	0.2507	8.56	3.51	0.98	0.46	385
C42	24.7	0.1235	0.2471	0.2023	0.2635	8.82	6.50	0.92	0.57	149
C43	24.8	0.1236	0.2471	0.2023	0.2643	8.79	6.33	0.95	0.57	166
C44	24.9	0.0986	0.1971	0.2036	0.2525	8.62	4.34	0.99	0.50	219

Table 1
(continued)

ID	T	Total Mg	Total Cl	Total C (DIC)	Total Na	pH	Ω	$log\left(\frac{a_{Mg^{2+}}}{a_{CO_3^{2-}}}\right)$	I	t_{ind}
#	°C	*mol/kgs*	*mol/kgs*	*mol/kgs*	*mol/kgs*				*mol/kgs*	*s*
45	24.9	0.1892	0.3784	0.2023	0.2364	8.14	3.39	1.91	0.78	447
46	24.8	0.1891	0.3781	0.2024	0.2384	8.13	3.32	1.93	0.78	407
47	25.2	0.1889	0.3778	0.2024	0.2324	8.04	2.91	1.98	0.78	617
D48	24.8	0.2984	0.5967	0.2024	0.2434	8.01	3.98	2.31	1.13	301
D49	24.8	0.2985	0.5970	0.2024	0.2434	8.00	3.91	2.32	1.13	296
D50	24.6	0.2984	0.5968	0.2025	0.2405	7.97	3.68	2.35	1.13	347
D51	25.0	0.2986	0.5971	0.2024	0.2364	7.92	3.41	2.39	1.14	510
D52	24.8	0.2986	0.5971	0.2024	0.2334	7.90	3.27	2.42	1.13	591
E53	25.1	0.4499	0.8998	0.2023	0.2626	7.88	4.52	2.73	1.64	233
E54	25.0	0.4499	0.8998	0.2024	0.2620	7.88	4.50	2.73	1.64	240
E55	24.3	0.4156	0.8312	0.1990	0.2236	7.72	3.13	2.83	1.52	1104
E56	24.9	0.4158	0.8317	0.1989	0.2235	7.67	2.87	2.87	1.52	1432
E57	24.1	0.4160	0.8320	0.1990	0.2235	7.67	2.85	2.88	1.52	1499
E58	24.8	0.4158	0.8317	0.1989	0.2235	7.66	2.81	2.89	1.52	1821
E59	24.5	0.4160	0.8320	0.1990	0.2235	7.66	2.81	2.89	1.52	2333
Heterogeneous nucleation										
H60	25.0	0.0547	0.1095	0.2024	0.2228	8.48	2.20	0.84	0.370	3732
H61	25.1	0.0545	0.1090	0.2022	0.2163	8.33	1.72	1.01	0.368	13200
H62	24.8	0.0547	0.1093	0.2022	0.2163	8.33	1.72	1.02	0.368	16836
Error:										
	0.01	0.0001	0.0001	0.0001	0.0001	0.006	0.01	<0.01	<0.01	12.2%

eter), and the crystal morphology was observed by SEM (FEI company: XL-30 ESEM-FEG) at Yale University.

Determination of Induction Time

The induction time (t_{ind}) is defined as the period elapsed after the achievement of a supersaturated solution and before the appearance of detectable solid phases (Mullin, 2001). In our practice, the solution mixing times were not included in our estimated induction times. However, this choice is not critical, because if we were instead to include mixing times in our induction time estimates, the error should be in a range of 0.5∼9 percent depending on the length of induction time, which was within the uncertainty of the induction-time measurement (∼12%).

A relationship exists between the induction time (t_{ind}) and the nucleation rate (J), which depends on the detection method used in an experiment. Equation (6b) is applicable only if a detector can measure the number density of nuclei in solution. In this work, nucleation of crystal is detected by light scattering (Westin and Rasmuson, 2005; Shiau and Lu, 2014), which yields the number density directly.

To accomplish these measurements, a A4-paper-size background plate with 1×1 cm checkered pattern was placed behind the solution bottle (fig. 1). When light beams reflected from the white and black squares of the plate are passing through a solution that is free of particles, the contrast in light intensity received by the camera between them is recorded and defined as ΔI_i (i represents the number of pixels in camera

detector). When particles appear in solution, light beams scatter, and the intensity difference ΔI_i reduces. Integrating the intensity difference between each neighbored pixel pairs over the entire sampling region yields the total light intensity difference: $\Delta I_{tot} = \sum_i \Delta I_i$. Thus, a reduced ΔI_{tot} represents an increased particle number in solution. Equation (6b) is adopted to determine surface energy in our system (see Westin and Rasmuson, 2005). Details are summarized in Appendix II.

The Stability Field of Nesquehonite

The stability field of nesquehonite was calculated using IPhreeqc with standard thermodynamic data, and the result is shown in figure 3. Input parameters are temperature, solution pH, total Mg and DIC concentrations in mols per kilogram solution (mol/kgs), and output parameters include the activities of Mg^{2+} and CO_3^{2-}, the saturation indices (SI) of nesquehonite and brucite, as defined in the standard form:

$$SI = \log(\Omega) = \frac{\log IAP}{K_{sp}} \tag{24}$$

where IAP is ion activity product, $K_{sp,n}$ and $K_{sp,b}$ are solubility product of nesquehonite ($10^{-5.16}$, from Zhao and others, 2013) and brucite ($10^{-10.88}$, from Pitzer database), respectively. The Pitzer activity model and related parameters were adopted due to the relative high ionic strength of experimental solutions.

Figure 3 shows the stability fields of nesquehonite and brucite, and contours representing solutions having constant saturation states (Ω, solid curves) and constant Mg^{2+}/CO_3^{2-} activity ratios ($\log(a_{Mg^{2+}}/a_{CO_3^{2-}})$, dashed curves). As can be seen in figure 3, one can design experiments with specific saturation states and Mg^{2+}/CO_3^{2-} activity ratios in the nesquehonite stability field. Experimental pH values need to be measured in order to calculate the precise saturation state (see Appendix I).

In experiments conducted near the brucite-nesquehonite phase boundary, solutions sometimes became turbid during solution mixing due to the precipitation of brucite. These experiments were stopped immediately and discarded. Moreover, near the boundary of nesquehonite saturation at lower pH (Ω = 1.00 line in fig. 3), the nucleation rates were often so low that there was no significant change in physical or chemical parameters which could be used to separate nucleation from growth, making induction time measurement unreliable. These experiments were also discarded.

RESULTS

As a typical example, figure 2 depicts the evolution of solution pH and total light intensity difference (ΔI_{tot}) for experiment D51 (also shown in table 1). The experiment has been divided into three periods. Period P1 represents the initial condition of the $NaOH$-$NaHCO_3$-H_2O solution mixture. Upon the introduction of $MgCl_2$ solution at the end of P1, there was a sharp pH decrease and a dramatic change in the solution transparency, after which the pH value of the solution became stable again (P2). This period of stability was followed by Period P3 with gradual decline in both solution pH and ΔI_{tot}. At the early stage of P2, supersaturation of solution relative to nesquehonite can be established at the moment when solution transparency and pH value reach constant values. Upon mixing, pH values and densities of the solution fluctuate, as shown in figure 2. The stable pH and density values (as reflected in ΔI_{tot}) indicate the presence of a transparent homogeneous solution. Furthermore, stage P3 could be further divided into two subsections (P3' and P3") according to the noticeable decline of solution pH values. In period P3', the solution pH is constant while ΔI_{tot} decreases significantly. One experiment was repeated six times under very similar conditions (B22-B27 in table 1), to determine the uncertainty in our pH and saturation state

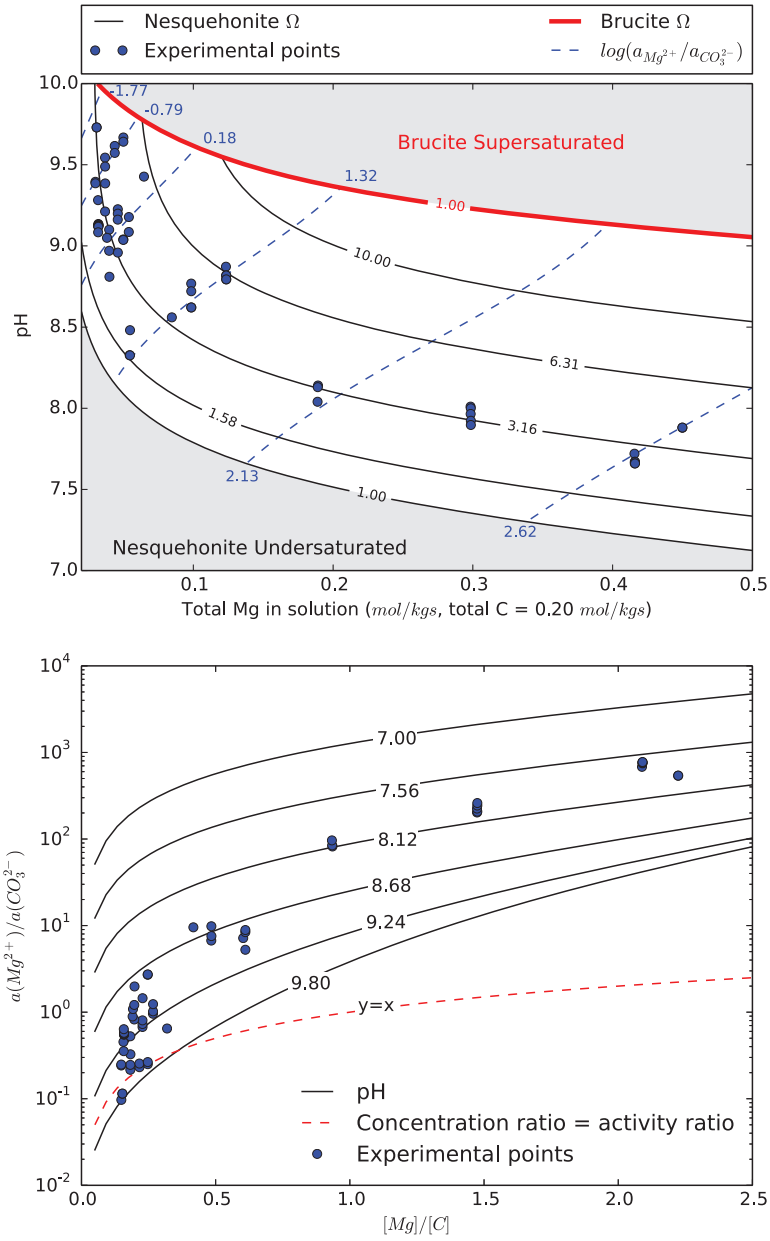

Fig. 3. Top panel: Relationship between pH and Mg concentration in solution. The saturation index (SI) and Mg^{2+}/CO_3^{2-} activity ratio contour generated by geochemical code, IPhreeqc. The dots mark compositions of the experimental solutions, in which precipitation experiments were conducted. They are in the region where nesquehonite is super-saturated, but brucite is undersaturated. Solutions having similar $\log(a_{Mg^{2+}}/a_{CO_3^{2-}})$ values and different saturation indices were grouped and compared. Bottom panel: Relationship between Mg^{2+}/CO_3^{2-} activity ratio and Mg/DIC concentration ratio under various pHs.

measurements (n = 6; pH = 9.126 ± 0.006). This uncertainty, when propagated through the calculations, results in a slight variation in the saturation state of nesquehonite (Ω = 2.72 ± 0.01).

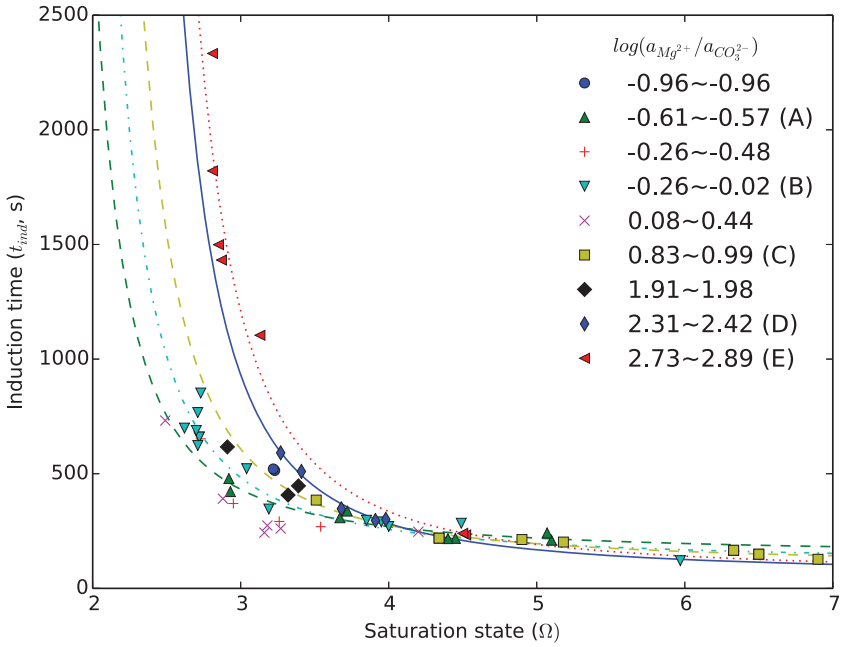

Fig. 4. Measured nesquehonite induction times in different solutions as a function of saturation states. The curves are the fitted using classic nucleation theory (CNT) with different surface energies.

A total of 62 precipitation experiments were carried out in this study. The experimental conditions and induction time estimates are listed in table 1, grouped from A through E. The measured t_{ind} is, in general, inversely correlated with the saturation state (Ω), despite the variation in Mg^{2+}/CO_3^{2-} activity ratios. At high saturation state ($\Omega > 4$), the induction time is little affected by solution chemistry. For instance, the induction times in experiments #B16, #C40, and #E54 with similar saturation states (Ω = 4.49, 4.34, 4.50) but different $\log(a_{Mg^{2+}}/a_{CO_3^{2-}})$ ratios (−0.02, 0.99, 2.73) are 284 s, 219 s, and 240 s, respectively. In contrast, at low saturation states ($\Omega < 4$), activity ratios have a strong influence on t_{ind} (fig. 4): that is, the bigger the $\log(a_{Mg^{2+}}/a_{CO_3^{2-}})$ value, the longer the induction time. For example, experiments #A10, #13, #33, #47, and #E56 have virtually constant saturation states (Ω = 2.61 ± 0.03) but $\log(a_{Mg^{2+}}/a_{CO_3^{2-}})$ ratios between −0.60 and 2.73. The induction time first decreases from 479 s to 370 s, and then increases to 1104 s.

The calculated charge imbalances between cations and anions are mainly caused by errors associated with thermodynamic parameters, is also given by IPheeqc program. They show that most relative charge errors are ±2 percent with a maximum value of 8.23 percent. These uncertainties do not affect our modeling and discussion in following sections.

The XRD and SEM results of final solid products from three experiments are shown in figure 5. The XRD patterns match those of natural nesquehonite crystals, and SEM images show the rod-like habitat of nesquehonite crystals.

DISCUSSION

Our experiments clearly indicate that solution chemistry could change the energy barrier for nucleation, especially at low saturation states. In this section, we interpret

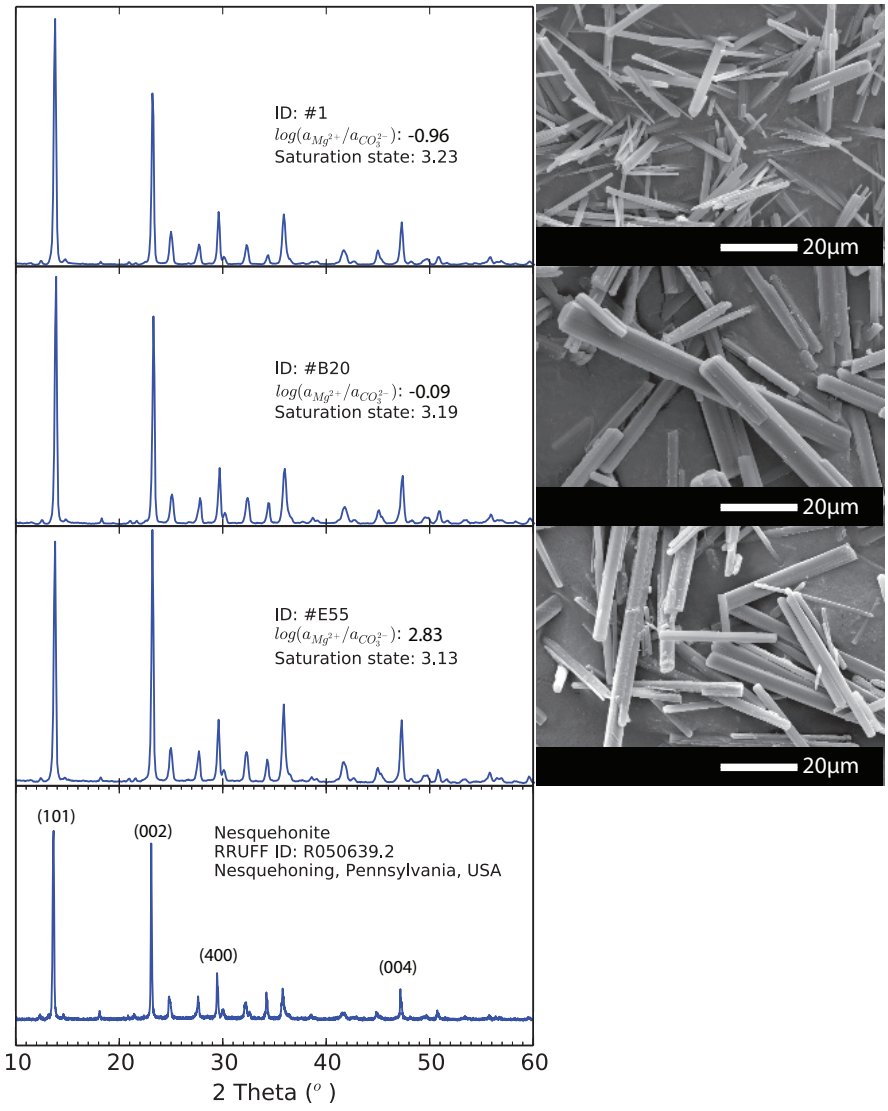

Fig. 5. XRD patterns and SEM images of three solid products with typical initial solution chemistry. All XRD peaks match those of nesquehonite from RUFF^{TM} (a high quality mineral spectral database).

our data using the CNT and then discuss two factors that may affect the results: ion absorption and surface charge on the nuclei.

Induction Time and Surface Energy

The CNT provides a link between induction time and surface energy, as expressed in equation (7). To first order, fitting our experimental data to the form of equation (7) yields two statistically significant straight lines (fig. 6): one dashed line passes through rectangles (Group-I in fig. 6A) with a relatively shallow slope, and the other solid straight line passes through a large number of closed symbols with a steeper slope (Group-II, fig. 6A). Similar to several previous studies (Mullin and Ang, 1976; Söhnel

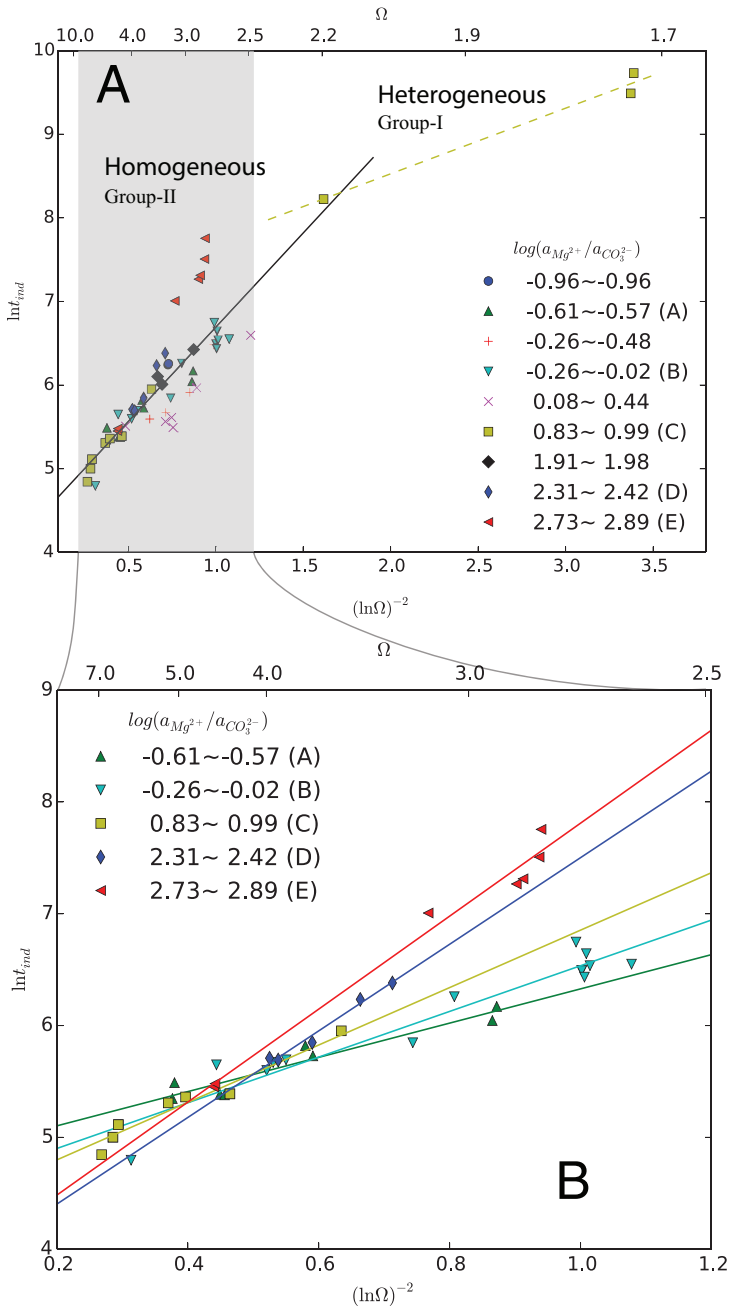

Fig. 6. Top panel: (A) The relationship between $\ln(t_{ind})$ versus $(\ln(\Omega))^{-2}$. Experiments with saturation state Ω higher than 2.20 ($(\ln(\Omega))^{-2} < 1.62$) are considered to indicate homogeneous nucleation region, which has been highlighted in fig. 6B. The scattered induction time data suggest varied surface energy predicted by CNT. Bottom panel: (B) Plot of $\ln(t_{ind})$ versus $(\ln(\Omega))^{-2}$ at different $\log(a_{Mg^{2+}}/a_{CO_3^{2-}})$ ratios. The fitted slopes, intercepts and R^2 values are given in table 2.

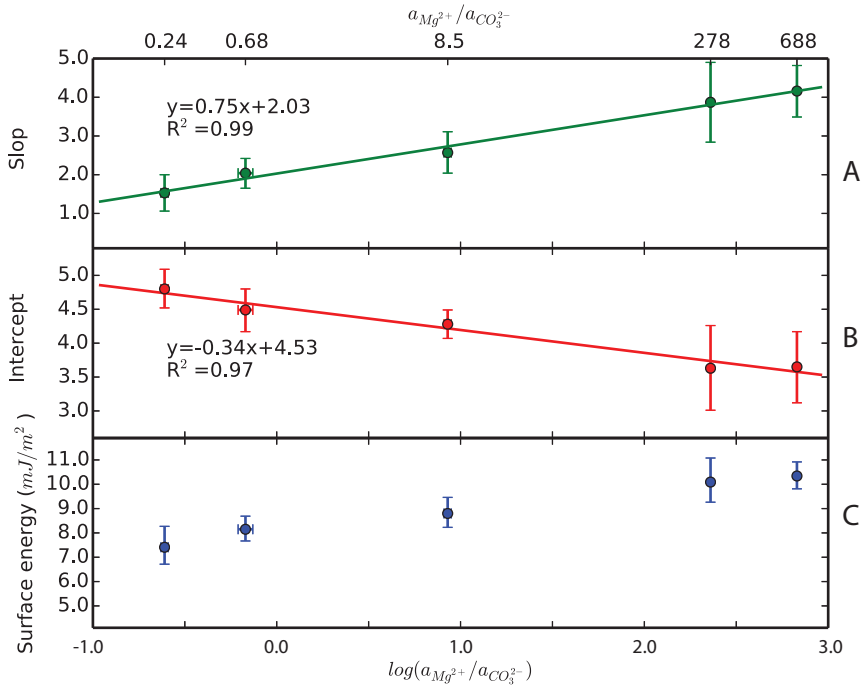

Fig. 7. The variation of fitting parameters (A: slopes; B: intercept; C: surface energy assuming spherical nuclei shape) as a function of $\log(a_{Mg^{2+}}/a_{CO_3^{2-}})$.

and Mullin, 1978; Waly and others, 2012; Qin and others, 2016), the change of slope between two fitted lines can be interpreted to indicate a shift from heterogeneous (shallow slope) to homogenous nucleation (steep slope). However, a careful look at Group-II data (especially for those at low saturation states) in the homogeneous nucleation domain reveals scatter (fig. 6B) that is beyond the analytical error (~12.2%) of the induction-time measurements. Moreover, among samples with a similar $\log(a_{Mg^{2+}}/a_{CO_3^{2-}})$ ratio in each of five groups, a better correlation (R^2 = 0.91-0.98) between $\ln(t_{ind})$ versus $(\ln(\Omega))^{-2}$ can be found and is shown in figure 6B. The slope of the correlation increases from 1.53 to 4.16 and the intercept decreases from 4.80 to 3.65, with increasing $\log(a_{Mg^{2+}}/a_{CO_3^{2-}})$ ratios (from -0.61–2.83, also in fig. 7).

Equations (4) and (7) state that at a given saturation state, temperature, and geometric factors, the slope of correlation between $\ln(t_{ind})$ versus $(\ln(\Omega))^{-2}$ shall be a constant, which corresponds to surface energy. Table 2 lists the calculated surface free energy values using spherical shape factors. It shows increasing slope (surface energy of nesquehonite, γ) and decreasing intercept in the correlation with increasing $\log(a_{Mg^{2+}}/a_{CO_3^{2-}})$ ratios (fig. 7).

In this work, we used the $\log(a_{Mg^{2+}}/a_{CO_3^{2-}})$ ratio as an index to describe the solution stoichiometry. Figure 3B shows that the Mg^{2+}/CO_3^{2-} activity ratio is very sensitive to solution pH, which could be several orders of magnitude higher than Mg/DIC concentration ratio, making the $\log(a_{Mg^{2+}}/a_{CO_3^{2-}})$ ratio a suitable experimental variable.

Surface Absorption and the Surface Energy of Nesquehonite

In our experiments, the $\log(a_{Mg^{2+}}/a_{CO_3^{2-}})$ ratio of solution strongly affects the surface energy (γ) since the temperature variation in our experiment is small and

Table 2

Surface free energy, γ, calculated through $ln(t_{ind}) - (ln(\Omega))^{-2}$ slope assuming spherical nuclei

Group	A	B	C	D	E
$\log(a_{Mg^{2+}}/a_{CO_3^{2-}})$[a]	-0.61 (0.03)	-0.17 (0.08)	0.93 (0.06)	2.36 (0.05)	2.83 (0.07)
Slope	1.53	2.04	2.57	3.87	4.16
Upper bound[b]	2.01	2.43	3.10	4.90	4.83
Lower bound	1.06	1.66	2.03	2.84	3.50
Intercept	4.80	4.49	4.28	3.63	3.65
Upper bound	5.08	4.81	4.49	4.25	4.18
Lower bound	4.51	4.18	4.07	3.00	3.13
Goodness of fit (R^2)	0.91	0.92	0.94	0.98	0.98
Shape	surface energy (mJ/m^2, 298K)				
Spherical	7.41	8.15	8.80	10.09	10.34
Plus	9.4%	5.9%	6.5%	8.2%	5.1%
Minus	12%	6.6%	7.5%	9.8%	5.6%

[a] The average activity ratio taken from all experiments in one group; number in bracket was activity ratio standard error.
[b] The upper and lower bounds are taken based on 95% confidence interval.

because the nuclei are spherical. Foreign particles can also affect induction time by introducing heteronucleation sites. We reject this possibility because results with similar Mg^{2+}/CO_3^{2-} activity ratios yielded reproducible results that follow the CNT prediction. Thus, we believe surface energy is responsible for the slope shift in the relationship of $\ln(t_{ind})$ versus $(\ln(\Omega))^{-2}$, rather than the introduction of foreign particles as heteronucleation sites.

The change of surface energy could result from different surface energy excesses caused by absorption of ions from solution. One possible situation is that increasing CO_3^{2-} concentration in solution promotes the absorption of CO_3^{2-} onto nuclei surfaces, and thereby reducing the surface energy. However, increasing Mg^{2+} concentration does not noticeably reduce surface energy (fig. 7). This can be understood at least qualitatively from both energetic and kinetic perspectives.

From an energy perspective, adding a layer of CO_3^{2-} ions will require much less energy than adding a layer of Mg^{2+} ions in nesquehonite crystal lattice. In aqueous solution, CO_3^{2-} ion has about three water molecules in the first hydration shell (Tongraar and others, 2011), whereas Mg^{2+} holds six water molecules in its first hydration shell. In order for CO_3^{2-} ions to enter the crystal lattice of nesquehonite, it needs to lose two of the three water molecules, requiring 73.94 kcal/mol energy (Tongraar and others, 2011), which is much less than 103.73 kcal/mol needed for Mg^{2+} ions to lose four of its six water molecules in its first hydration shell (Rodriguez-Cruz and others, 1999) in order to enter nesquehonite crystal lattice. This energy difference indicating less barrier for CO_3^{2-} transferring from solution to solid.

From a kinetic perspective, CO_3^{2-} ions are more readily adsorbed onto nesquehonite mineral surfaces. All atoms in a CO_3^{2-} ion and the three water molecules in its first water shell are located in the same plane (that is, no water molecule is tightly bound with CO_3^{2-} ion from above or below the plane), whereas six water molecules tightly bounded with a Mg^{2+} form an octahedron (Bruneval and others, 2007; Tongraar and others, 2011). Thus, there is a chance that CO_3^{2-} can be absorbed onto mineral surfaces without losing water in the first water shell before it can enter crystal

TABLE 3

Intrinsic constants of different surface reactions on magnesium carbonate mineral surfaces using two different surface charge-electric potential dependencies

	Magnesite[c]	Nesquehonite[d]	
Surface reactions	Log *KM*	Log *KN*(1)	Log *KN*(2)
(1) $>CO_3H^0 = >CO_3^- + H^+$	-4.65	-4.04	-4.40
(2)$>CO_3H^0 + Mg^{2+} = >CO_3Mg^+ + H^+$	-2.2	-4.15	-1.18
(3)$>MgOH^0 = >MgO^- + H^+$	-12	-12	-12(fixed)
(4)$>MgOH^0 + H^+ = >MgOH_2^+$	10.6	11.3	11.5
(5)$>MgOH^0 + CO_3^{2-} + H^+ = >MgCO_3^- + H_2O$	14.4	15.3	19.3
(6) $>MgOH^0 + CO_3^{2-} + 2H^+ = >MgHCO_3^0 + H_2O$	22.4	22.4	22.4(fixed)
Model	Constant Capacitance	SDL-1	SDL-2
Site density ($\Gamma_{>Mg^+} = \Gamma_{>CO_3^-}, mol \cdot m^{-2}$)	9.00×10^{-6}	9.56×10^{-6}	9.72×10^{-6}

[c] From Pokrovsky and others (Pokrovsky and others, 1999).
[d] From this study.

lattice, minimizing hydrophobic area in aqueous solution (Bruneval and others, 2007), whereas absorbing Mg^{2+} onto mineral surface requires breaking at least one Mg-OH_2 bond. Even if CO_3^{2-} ion loses two water molecules as it is absorbed onto mineral surface, it will not prevent other CO_3^{2-} ions from occupying neighboring positions since the residual water does not interact with neighboring CO_3^{2-} ions. In contrast, absorbing Mg^{2+} with some tightly bound waters will prevent other cation from occupying neighboring sites, increasing surface energy. Such absorption poisoning has been identified in the crystal growth of calcite in Mg-containing solutions (Berner, 1975; Deleuze and Brantley, 1997).

Notably, figure 7 suggests that the barrier energy for monomer attachment (E_A) (eq. 7) may be reduced in high surface energy conditions since the intercept of $\ln(t^{ind})$-$(\ln(\Omega))^{-2}$ plot is inversely proportional to surface energy, although other interpretations cannot be ruled out.

Modeling Surface Charge Effect on Surface Energy of Nesquehonite

Equation (17) states that the surface energy of a particle is composed of two components: one derives from the atoms on the surface and the other arises from electric potential energy because the interface is charged and in a dielectric medium. As discussed above, selective absorption of CO_3^{2-} and Mg^{2+} could result in the change of surface energy. In addition, the absorption of charged ions could induce surface charging and reduce particle surface energies, thereby altering the electric potential distribution away from the interface. Thus, changes of surface charge will also alter surface energy. For example, a higher concentration of CO_3^{2-} and OH^- (than that of Mg^{2+}) will lead to more negative surface charge density on nuclei surface and a decrease in surface energy.

Both absorption and the electrostatics of the surface can be described by a surface complexation model (SCM), which was originally developed for carbonates by Van Cappellen and others (1993) and later was applied to other carbonate surfaces (for example Pokrovsky and Schott, 2002). This model implies that there exists two initial species (sites) $>Mg^+$ and $>CO_3^-$ exposed on the cleavage plane of magnesium carbonates which are present in equal densities $\Gamma_{>Mg^+}=\Gamma_{>CO_3^-}$. When immersed in aqueous solution, two initial sites are hydrated to form two major hydration species $>MgOH^0$ and $>CO_3H^0$ (Pokrovsky, 1998). Ion-pairing and hydrolysis on the nesque-

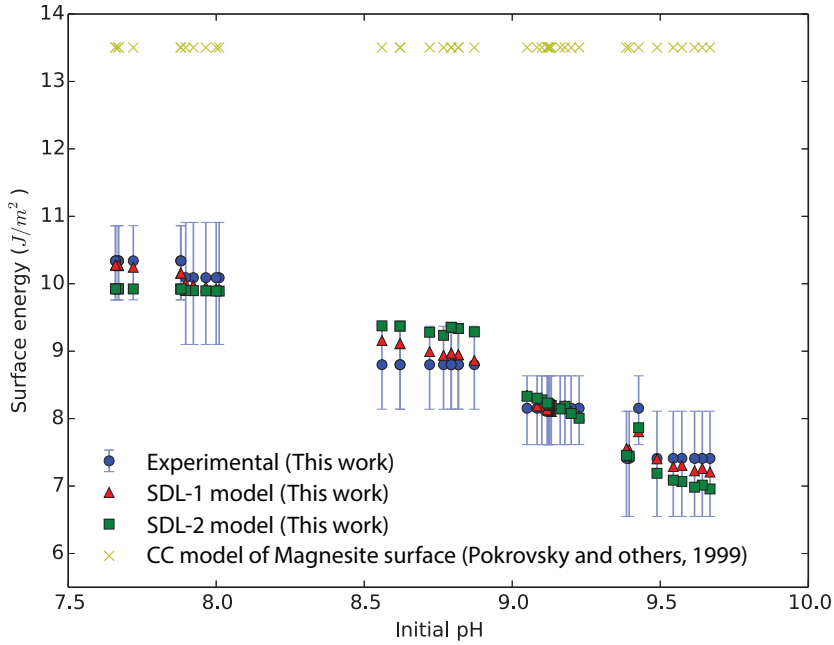

Fig. 8. Comparison between the experimentally determined surface energy of nesquehonite nuclei, the surface energies calculated for nesquehonite and the surface energies calculated for magnesite, using different models and parameters. The SDL-1 model exhibited the sum of squares due to error (SSE) of 1.02 and SDL-2 model 5.25.

honite surface leads to additional surface species including: $>MgOH_2^+$, $>MgOH^0$, $>MgO^-$, $>MgCO_3^-$, $>MgHCO_3^0$, $>CO_3H^0$, $>CO_3^-$ and $>CO_3Mg^+$. These eight species relate to one another by six reactions (table 3).

If nesquehonite nuclei surfaces are assumed to behave like magnesium carbonate, and the crystalline water present in nesquehonite has a negligible contribution to overall surface complexation, then surface reactions and the intrinsic stability constants of nesquehonite can be calculated after the following assumptions:

1) The stability constants of these reactions 3 and 6 in table 3 on nesquehonite nuclei surface are fixed at the same values as those on magnesite nuclei surface. This assumption is justified because of the low concentration of $>MgO^-$ and small variations of the neutral $>MgHCO_3^0$ complex at our experimental pH range of 7.66 to 9.80 (Pokrovsky and others, 1999; Pokrovsky and Schott, 2002). These species make insignificant contributions to the overall surface energy.

2) The chemical contribution term in equation (17) is assumed constant: $\sum_i \Gamma_i = \Gamma_{>Mg^+} + \Gamma_{>CO_3^-}$.

3) The surface-charge density σ_0 is estimated as follows:

$$\sigma_0 = \sum_i z_i e \Gamma_i \tag{25}$$

where z_i represents the valence of surface species i, and e is elementary electric charge.

With these assumptions, two electric double layer (SDL-1 and SDL-2) models were tested (eqs. 22-23). The electrostatic contribution to surface energy in equation (17) is calculated by integrating equations (22) and (23). The electrostatic contribution to

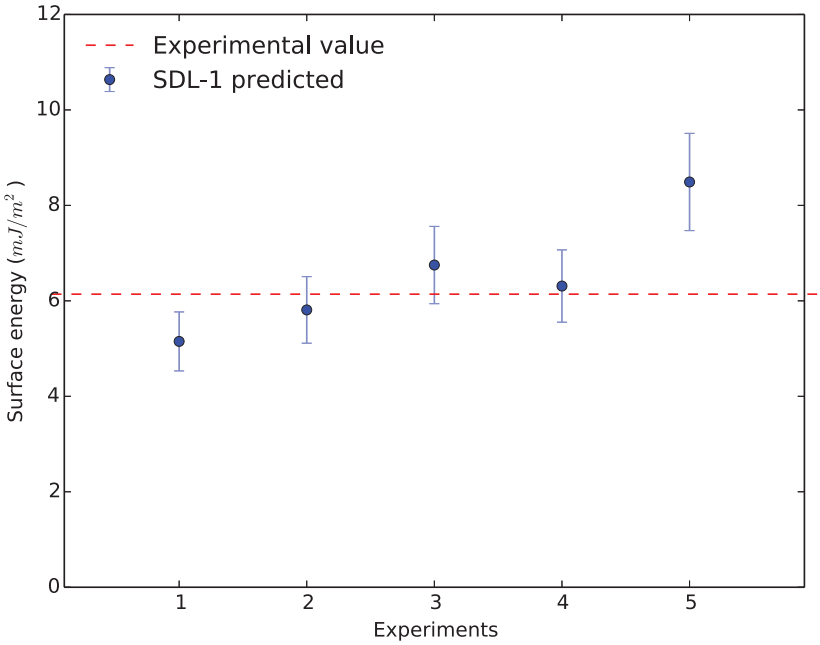

Fig. 9. Comparison between the surface energy measured in previous studies (6.14 mJ/m^2, Zhao and others, 2013) and that predicted by the SDL-1 model. All parameters used to reproduce previous results are from this study. The error bar was estimated using the largest error in the surface-energy measurement.

surface energy on the nuclei is the most important factor. Surface complexation reactions are solved simultaneously with the solution speciation. Speciation kinetics are assumed to be fast. All five groups of experiments (#A-#E), each of which has a similar Mg^{2+}/CO_3^{2-} activity ratio but different saturation states and pH values, are used to establish the model.

The parameters derived by fitting two different electric double layer (EDL) models of nesquehonite nucleation at ~25 °C are listed in table 3, where they are also compared with values for magnesite, which were extracted using potentiometry (Pokrovsky and others, 1999). The intrinsic reaction constants for surface reactions (4 through 6) related to the Mg-based surface site ($>Mg^+$) are much bigger than those of other reactions, suggesting that the Gibbs energy released by forming $>MgOH_2^+$, $>MgCO^{3-}$ or $>MgHCO_3^0$ species is higher than the formation of $>CO_3^-$ or $>CO_3Mg^+$ species, which is consistent with the idea that Mg^{2+} absorbs more extensively than CO_3^{2-} to the surface because it has a different hydration structure and energy.

Figure 8 shows fitting results for the SDL-1 and SDL-2 models (eq. 25). Because ionic strengths in our experiments are high, the SDL-1 model is more suitable to describe the relationship between charge density and electric potential. Our results suggest a value of 9.56-9.72 $\times$ 10^{-6} mol $\cdot$ m^{-2} for the site density (that is $\Gamma_{>Mg^+} = \Gamma_{>CO_3^-} = 9.56-9.72 \times 10^{-6}$ mol $\cdot$ m^{-2}) of the nesquehonite surface, which is slightly higher than that of magnesite ($\Gamma_{>Mg^+} = \Gamma_{>CO_3^-} = 9.00 \times 10^{-6}$ mol $\cdot$ m^{-2}), but more than the one inferred through crystallographic data of nesquehonite ($\Gamma_{>Mg^+} = \Gamma_{>CO_3^-} = 4.0-8.0 \times 10^{-6}$ mol $\cdot$ m^{-2} depending on where the interface plane is chosen).

Our surface-charge model assumes that the surface is saturated and that no extra absorption occurs; that is, the surface charge variation is independent of surface

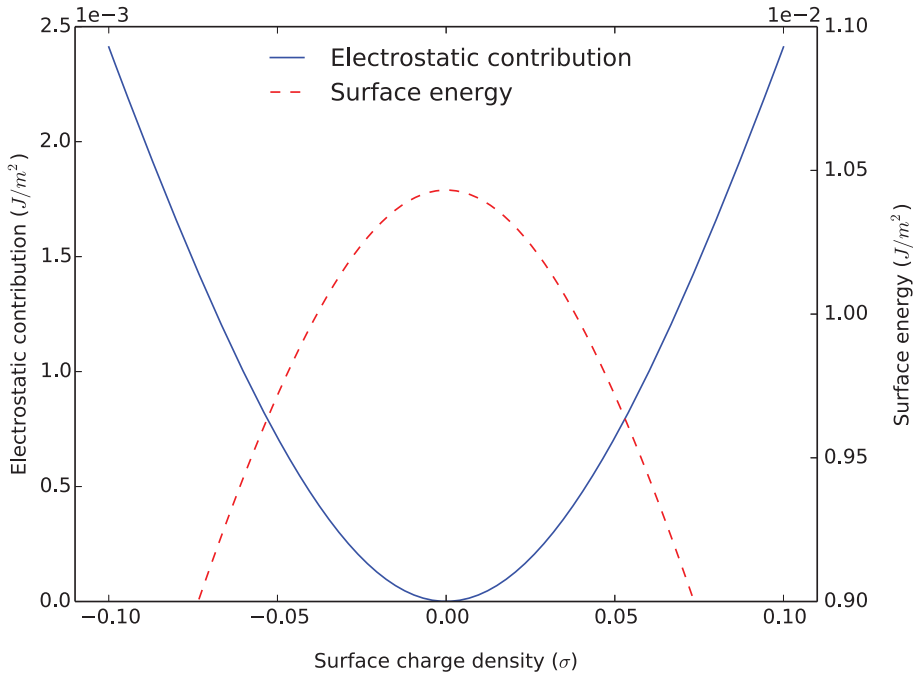

Fig. 10. Plot of electrostatic contribution $\int_0^{\Psi_0}\sigma(\Psi)d\Psi$ on nuclei surface energy (γ) as a function of surface charge densities (σ). When σ is 0, the surface energy cannot be reduced by attracting counterions and reaches its maximum value (298K, I = 0.5 mol/kgs).

absorption. However, in real cases, it is conceivable that surface absorption should cause changes in surface charge as well. Moreover, the SCM may provide little information about the physical surface process that controls surface energy of solid, since different surface models can describe the same experimental phenomenon (for example Kulik, 2009, 2002).

Model Implication

Our model to calculate surface energy can also be tested by experiments published previously (fig. 9). Five experiments precipitating nesquehonite from aqueous solutions were reported by Zhao and others (2013). Saturation states of the solutions were calculated by considering the total concentration of DIC (0.1–0.4 mol/L) and Mg (0.017–0.034 mol/L), and pH values (9.01–9.51). The CNT predicts all five experiments shall have nuclei with the same surface energy (6.14 mJ/m^2), whereas our surface-energy model yields slightly different surface energies, three of which agree with the experimental values within analytical uncertainty (in fig. 9).

If surface charge controls surface energy, then the modeling result can predict the p.z.c. of nesquehonite. Equation (15) implies that the surface energy will reach a maximum value when the electrostatic contribution is zero (fig. 10), and the energy barrier for nucleation is reduced when surface charge deviates away from the p.z.c. Figure 8 shows that the surface energy of nesquehonite nuclei reaches the maximum when pH = 7.66, indicating the p.z.c occurs when pH $\leq$ 7.66, which is lower than that of magnesite (pH $\approx$ 8.0, Pokrovsky and others, 1999).

Our results can also be applied to heterogeneous nucleation. For example, Giuffre and others (2013) investigated the heterogeneous nucleation of calcite on

high-purity polysaccharide substrates that had different functional groups. They used the surface charges of substrates in air to indicate the surface energies in water, assuming that the highly charged functional cause high surface energies in air, but will be reduced in water by interacting with water. One of the substrates, chitosan, exhibits the lowest energy barrier for nucleation of calcite, and that the near-neutral chitosan has the highest surface energy in water, indicating lower energy barrier (γ_{net}) for heterogeneous nucleation ($\gamma_{net} = \gamma_{CaCO_3/solution} + h(\gamma_{CaCO_3/substrate} - \gamma_{substrate/solution})$) (Giuffre and others, 2013). This discovery is also consistent with our model.

CONCLUSION

Our study indicates that it is possible to estimate realistic mineral surface energies in solution by considering surface absorption and/or surface charging that arise from changes in solution chemistry. However, in order to predict the nucleation rate, parameters that are difficult to estimate, such as the concentration of monomers around the critical nucleus and energy barrier for monomer attachment, must be known.

The experimental data shows that variable surface energies exist on nuclei precipitating from solutions with different solution compositions but similar saturation states. These observations can be explained by selective absorption of CO_3^{2-} onto the nuclei surfaces. The resulting negative surface charge reduces surface energy by minimizing the electric potential energy and by affecting the diffuse layer where counterions are attracted. Under the assumptions laid out above, our model implies that neutral nuclei have the highest surface energy while charged surfaces are more stable. High surface energies favor the attachment of growth monomers. Since mineral precipitation in natural environments typically occurs under very low saturation states, this study highlights the importance of mineral-water interface chemistry under low chemical driving forces.

ACKNOWLEDGEMENTS

The authors wish to thank three anonymous reviewers, Associate Editor William Casey and Professor Henry Teng, for constructive reviews and helpful suggestions. Professor Casey is particularly thanked for the help on editing and resolving language issues. This work is supported by DOE Award (No.: DE-FE0004375) to Z.W., the National Natural Science Foundation of China (Grant No: 41528301 to Z.W. and Grant Nos. 41002014 and 41273075 to L.Z.), and a state scholarship grant from China Scholarship Council (CSC) to C.Z.

APPENDIX I

EXPERIMENTAL PROCEDURE OF SOLUTION PREPARATION

Following the calculation results shown in figure 3, it is theoretically feasible to design experiments with specific saturation states and Mg^{2+}/CO_3^{2-} activity ratios in the nesquehonite stability field. However, these experimental designs are difficult to implement because pH values in figure 3 were calculated based on charge balances in IPhreeqc module, and even a small uncertainty in thermodynamic data and/or any other parameter could yield a big difference in the calculated pH value. Thus, experimental pH values are needed in order to calculate the precise saturation state and Mg^{2+}/CO_3^{2-} activity ratios.

In practice, an iteration procedure, as illustrated in figure A1, was used to prepare solutions with various saturation states and Mg^{2+}/CO_3^{2-} activity ratios. For example, m_{Mg} gram of $MgCl_2$ stock solution (~1 mol/kgs) and m_{w1} gram of water ($m_{w1} + m_{w2} = m_w$) were first mixed to make solution A. After thermal equilibrium, the mixture was then added with solution B made by ~8.5 gram of $NaHCO_3$, m_{OH} gram of NaOH and m_{w2} gram of MQ water to achieve supersaturation. When the induction-time measurement was finished, the measured pH value was then used to calculate the practical saturation state and Mg^{2+}/CO_3^{2-} activity ratio. If the calculated Ω and Mg^{2+}/CO_3^{2-} activity ratio did not meet the desired values, different masses of water, NaOH and $MgCl_2$ stock solutions were used to make another solution. This process

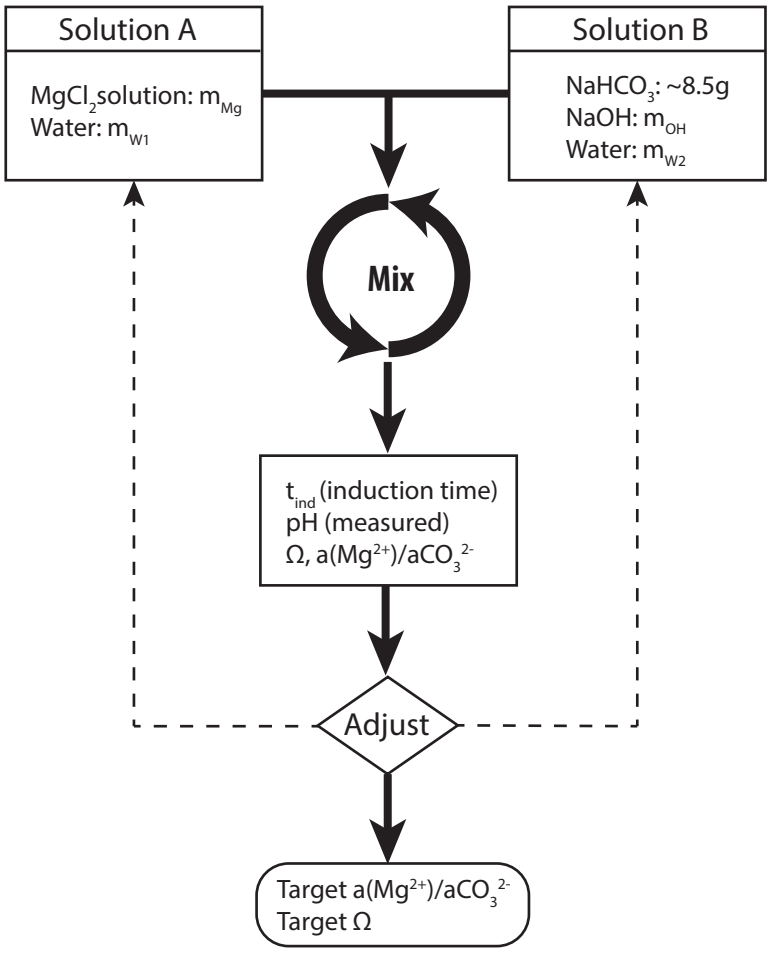

Fig. A1. Flow chart for solution preparation.

continued until the solution from one experiment obtained the target Ω value and Mg^{2+}/CO_3^{2-} activity ratio. All experiments conducted in this study are plotted figure 3.

APPENDIX II

DETAILED DATA PROCESSING TO OBTAIN INDUCTION TIME

When nucleation began, background objects became fuzzy due to light scattering through tiny crystal nuclei, leading to lower ΔI_{tot} values. A series of digital pictures were taken at a supersaturated solution with a constant background over the course of the experiment, and were then processed according to flowing procedures: 1) images with the RGB color model were converted to gray scale; 2) The brightness contrast between each pixel and its right side neighbor was calculated. These differences were summed and normalized to unit scale to define an index for ΔI_{tot}; 3) ΔI_{tot} data in the time series were smoothed by a low-pass filter to remove high frequency noise; and 4) the first derivation of the filtered ΔI_{tot} curve, representing the rate of transparency loss, was calculated (Zhao and others, 2013).

A sample $\Delta I_{tot} - t$ curve in figure 2 shows that there is no clear transition of ΔI_{tot} from the nucleation stage (P2) to the growth stage (P3), making it necessary to choose an arbitrary threshold to mark this transition. To do so, standard deviations of induction-time measurements in six experiments, with nearly the same

recipes (Experiments B22 through B27 in table 1) were calculated to give different thresholds. A threshold of $-0.00025\ s^{-1}$corresponds to the smallest error in these experiments, which is about 12.2 percent of the average induction time (707 ± 86s). This threshold was adopted for processing all our data.

The induction time of crystal nucleation in solution has been measured by many other techniques, including 1) visual observation (Söhnel and Mullin, 1982; Lohani, ms, 2006; Wikstrom, ms, 2007; Zhang and others, 2008; Qin and others, 2016); 2) pH variations (Rushdi and others, 1992; Waly and others, 2012); 3) conductivity variations (Lyczko and others, 2002; Isopescu and others, 2010; Zhao and others, 2013); 4) light transmittance (Westin and Rasmuson, 2005); 5) turbidity variations (Shiau and Lu, 2014); 6) video-image processing (Brown and Ni, 2012); 7) ultra-sound velocity (Omar and Ulrich, 2006); 8) Raman spectrum (Hänchen and others, 2008); 9) monitoring changes in ion activities (Olsson, 1995). Induction times measured by these techniques will have different values due to differences in detection sensitivity, but previous studies showed that the surface energy inferred from the experiments are similar. For example, in the studies of induction time of $CaCO_3$ nucleation in pure water, a surface energy of ~40.7 mJ/m^2 is obtained for calcite at 25°C by monitoring pH-drop (Gómez-Morales and others, 1996), 37.3 ± 0.4 mJ/m^2 for monitoring *in situ* calcium activities (Verdoes and others, 1992), and 37.8 ± 0.56 mJ/m^2 by detecting light transmittance drops (Westin and Rasmuson, 2005). Measurements of surface energy by different authors and technique shows that the surface energy estimates are insensitive to the method of measuring induction times.

REFERENCES

Berner, R. A., 1975, The role of magnesium in the crystal growth of calcite and aragonite from sea water: Geochimica et Cosmochimica Acta, v. 39, p. 489–504, http://dx.doi.org/10.1016/0016-7037(75)90102-7

Brown, C. J., and Ni, X.-W., 2012, Determination of metastable zone width, mean particle size and detectable number density using video imaging in an oscillatory baffled crystallizer: CrystEngCommun, v. 14, p. 2944–2949, http://dx.doi.org/10.1039/c2ce06628a

Bruneval, F., Donadio, D., and Parrinello, M., 2007, Molecular dynamics study of the solvation of calcium carbonate in water: The Journal of Physical Chemistry B, v. 111, n. 42, p. 12219–12227, http://dx.doi.org/10.1021/jp0728306

Butkus, M. A., and Grasso, D., 1998, Impact of aqueous electrolytes on interfacial energy: Journal of Colloid and Interface Science, v. 200, n. 1, p. 172–181, http://dx.doi.org/10.1006/jcis.1997.5380

Davies, P. J., and Bubela, B., 1973, The transformation of nesquehonite to hydromagnesite: Chemical Geology, v. 12, n. 4, p. 289–300, http://dx.doi.org/10.1016/0009-2541(73)90006-5

Deleuze, M., and Brantley, S. L., 1997, Inhibition of calcite crystal growth by Mg^{2+} at 100 °C and 100 bars: Influence of growth regime: Geochimica et Cosmochimica Acta, v. 61, n. 7, p. 1475–1485, http://dx.doi.org/10.1016/S0016-7037(97)00024-0

De Yoreo, J. J., Gilbert, P. U. P. A., Sommerdijk, N. A. J. M., Penn, R. L., Whitelam, S., Joester, D., Zhang, H., Rimer, J. D., Navrotsky, A., Banfield, J. F., Wallace, A. F., Michel, F. M., Meldrum, F. C., Cölfen, H., and Dove, P. M., 2015, Crystallization by particle attachment in synthetic, biogenic, and geologic environments: Science, v. 349, n. 6247, http://dx.doi.org/10.1126/science.aaa6760

Dong, M., Cheng, W., Li, Z., and Demopoulos, G. P., 2008, Solubility and stability of nesquehonite ($MgCO_3{\cdot}3H_2O$) in NaCl, KCl, $MgCl_2$, and NH_4Cl solutions: Journal of Chemical and Engeering Data, v. 53, p. 2586–2593, http://dx.doi.org/10.1021/je800438p

Ferrini, V., De Vito, C., and Mignardi, S., 2009, Synthesis of nesquehonite by reaction of gaseous CO_2 with Mg chloride solution: Its potential role in the sequestration of carbon dioxide: Journal of Hazardous Materials, v. 168, n. 2–3, p. 832–837. http://dx.doi.org/10.1016/j.jhazmat.2009.02.103

Fischbeck, R., and Müller, G., 1971, Monohydrocalcite, hydromagnesite, nesquehonite, dolomite, aragonite, and calcite in speleothems of the Fränkische Schweiz, Western Germany: Contributions to Mineralogy and Petrolology, v. 33, n. 2, p. 87–92, http://dx.doi.org/10.1007/BF00386107

Giuffre, A. J., Hamm, L. M., Han, N., Yoreo, J. J. D., and Dove, P. M., 2013, Polysaccharide chemistry regulates kinetics of calcite nucleation through competition of interfacial energies: Proceedings of the National Academy of Sciences of the United States of America, v. 110, n. 23, p. 9261–9266, http://dx.doi.org/10.1073/pnas.1222162110

Gómez-Morales, J., Torrent-Burgués, J., and Rodríguez-Clemente, R., 1996, Nucleation of calcium carbonate at different initial pH conditions: Journal of Crystal Growth, v. 169, n. 2, p. 331–338, http://dx.doi.org/10.1016/S0022-0248(96)00381-8

Hänchen, M., Prigiobbe, V., Baciocchi, R., and Mazzotti, M., 2008, Precipitation in the Mg-carbonate system—effects of temperature and CO_2 pressure: Chemical Engeering Science, v. 63, n. 4, p. 1012–1028, http://dx.doi.org/10.1016/j.ces.2007.09.052

Hopkinson, L., Rutt, K., and Cressey, G., 2008, The transformation of nesquehonite to hydromagnesite in the system $CaO\text{-}MgO\text{-}H_2O\text{-}CO_2$: An experimental spectroscopic study: The Journal of Geology, v. 116, n. 4, p. 387–400, http://dx.doi.org/10.1086/588834

Hunter, R. J., 2001, Foundations of Colloid Science, 2nd edition: Oxford, New York, Oxford University Press, 816 p.

Isopescu, R., Mateescu, C., Mihai, M., and Dabija, G., 2010, The effects of organic additives on induction time and characteristics of precipitated calcium carbonate: Chemical Engeering Research and Design, v. 88, n. 11, p. 1450–1454, http://dx.doi.org/10.1016/j.cherd.2009.10.002

Jull, A. J. T., Cheng, S., Gooding, J. L., and Velbel, M. A., 1988, Rapid growth of magnesium-carbonate weathering products in a stony meteorite from Antarctica: Science, v. 242, n. 4877, p. 417–419, http://dx.doi.org/10.1126/science.242.4877.417

Kashchiev, D., and van Rosmalen, G. M., 2003, Review: Nucleation in solutions revisited: Crystal Research and Technology, v. 38, n. 7–8, p. 555–574, http://dx.doi.org/10.1002/crat.200310070

Kubota, N., Kobari, M., and Hirasawa, I., 2014, Effects of detector sensitivity and resolution on induction time reading: CrystEngComm, v. 16, n. 6, p. 1103–1112, http://dx.doi.org/10.1039/C3CE42019A

Kulik, D. A., 2009, Thermodynamic concepts in modeling sorption at the mineral-water interface: Reviews in Mineralogy and Geochemistry, v. 70, n. 1, p. 125–180, http://dx.doi.org/10.2138/rmg.2009.70.4

——— 2002, Gibbs energy minimization approach to modeling sorption equilibria at the mineral-water interface: Thermodynamic relations for multi-site-surface complexation: American Journal of Science, v. 302, n. 3, p. 227–279, http://dx.doi.org/10.2475/ajs.302.3.227

Langmuir, I., 1916, The constitution and fundamental properties of solids and liquids. Part I: Solids: Journal of the American Chemical Society, v. 38, n. 11, p. 2221–2295, http://dx.doi.org/10.1021/ja02268a002

Lohani, S., ms, 2006, Understanding nucleation processes in the crystallization of polymorphs: Ann Arbor, Michigan, ProQuest Information and Learning Company, 226 p.

Lyczko, N., Espitalier, F., Louisnard, O., and Schwartzentruber, J., 2002, Effect of ultrasound on the induction time and the metastable zone widths of potassium sulphate: Chemical Engineering Journal, v. 86, n. 3, p. 233–241, http://dx.doi.org/10.1016/S1385-8947(01)00164-4

Lyklema, J. J., 1991, Fundamentals of Interface and Colloid Science, 1st edition: London, New York, Boston, Academic Press, 736 p.

Lyklema, J. J., De Keizer, A., Fleer, G. J., and Stuart Cohen, M. A., 1995, Electric double layers, *in* Lykelma, J. J., editor, Fundamentals of Interface and Colloid Science, Solid-Liquid Interfaces, volume 2: Academic Press, p. 1–232, http://dx.doi.org/10.1016/S1874-5679(06)80006-1

Mersmann, A., 1990, Calculation of interfacial tensions: Journal of Crystal Growth, v. 102, n. 4, p. 841–847, http://dx.doi.org/10.1016/0022-0248(90)90850-K

Mullin, J. W., and Ang, H.-M., 1976, Nucleation characteristics of aqueous nickel ammonium sulphate solutions: Faraday Discussions of the Chemical Society, v. 61, p. 141–148, http://dx.doi.org/10.1039/dc9766100141

O'Connor, W. K., Dahlin, D. C., Rush, G. E., Gedermann, S. J., Penner, L. R., and Nilsen, D. N., 2005, Aqueous mineral carbonation: Mineral Availability, Pretreatment, Reaction Parametrics, and Process Studies: Final Report, US DOE, DOE/ARC-TR-04-002.

Olsson, L.-F., 1995, Induction time of precipitation of calcium carbonate: Journal of Molecular Liquids, v. 65–66, p. 349–352, http://dx.doi.org/10.1016/0167-7322(95)00829-4

Omar, W., and Ulrich, J., 2006, Solid liquid equilibrium, metastable zone, and nucleation parameters of the oxalic acid−water system: Crystal Growth & Design, v. 6, n. 8, p. 1927–1930, http://dx.doi.org/10.1021/cg060112n

Parks, G. A., 1990, Surface energy and adsorption at mineral/water interfaces; An Introduction: Reviews in Mineralogy and Geochemistry, v. 23, p. 133–175.

Pokrovsky, O. S., 1998, Precipitation of calcium and magnesium carbonates from homogeneous supersaturated solutions: Journal of Crystal Growth, v. 186, n. 1–2, p. 233–239, http://dx.doi.org/10.1016/S0022-0248(97)00462-4

Pokrovsky, O. S., and Schott, J., 2002, Surface chemistry and dissolution kinetics of divalent metal carbonates: Environmental Science & Technology, v. 36, n. 3, p. 426–432. http://dx.doi.org/10.1021/es010925u

Pokrovsky, O. S., Schott, J., and Thomas, F., 1999, Processes at the magnesium-bearing carbonates/solution interface. I. A surface speciation model for magnesite: Geochimica et Cosmochimica Acta, v. 63, n. 6, p. 863–880, http://dx.doi.org/10.1016/S0016-7037(99)00008-3

Power, I. M., Wilson, S. A., Thom, J. M., Dipple, G. M., and Southam, G., 2007, Biologically induced mineralization of dypingite by cyanobacteria from an alkaline wetland near Atlin, British Columbia, Canada: Geochemical Transactions, v. 8, n. 13, http://dx.doi.org/10.1186/1467-4866-8-13

Qin, S., Zhang, Y., and Zhang, Y., 2016, Nucleation and morphology of sodium metaborate dihydrate from NaOH solution: Journal of Crystal Growth, v. 433, p. 143–147. http://dx.doi.org/10.1016/j.jcrysgro.2015.10.012

Rodriguez-Cruz, S. E., Jockusch, R. A., and Williams, E. R., 1999, Hydration energies and structures of alkaline earth metal ions, $M^{2+}(H_2O)_n$, n=5−7, M =Mg, Ca, Sr, and Ba: Journal of the American Chemical Society, v. 121, n. 38, p. 8898–8906, http://dx.doi.org/10.1021/ja9911871

Rushdi, A. I., Pytkowicz, R. M., Suess, E., and Chen, C. T., 1992, The effects of magnesium-to-calcium ratios in artificial seawater, at different ionic products, upon the induction time, and the mineralogy of calcium carbonate: A laboratory study: Geologische Rundschau, v. 81, n. 2, p. 571–578, http://dx.doi.org/10.1007/BF01828616

Sayles, F. L., and Fyfe, W. S., 1973. The crystallization of magnesite from aqueous solution: Geochimica et Cosmochimica Acta, v. 37, n. 1, p. 87–99, http://dx.doi.org/10.1016/0016-7037(73)90246-9

Shiau, L.-D., and Lu, T.-S., 2014, A model for determination of the interfacial energy from the induction time or metastable zone width data based on turbidity measurements: CrystEngComm, v. 16, n. 41, p. 9743–9752, http://dx.doi.org/10.1039/C4CE01245C

Söhnel, O., and Mullin, J. W., 1978, A method for the determination of precipitation induction periods: Journal of Crystal Growth, v. 44, p. 377–382, http://dx.doi.org/10.1016/0022-0248(78)90002-7

——— 1982, Precipitation of calcium carbonate: Journal of Crystal Growth, v. 60, p. 239–250, http://dx.doi.org/10.1016/0022-0248(82)90095-1

Tongraar, A., Yotmanee, P., and Payaka, A., 2011, Characteristics of CO_3^{2-}–water hydrogen bonds in

aqueous solution: Insights from HF/MM and B3LYP/MM MD simulations: Physical Chemistry Chemical Physics, v. 13, p. 16851–16860, http://dx.doi.org/10.1039/c1cp21802f

Van Cappellen, P., Charlet, L., Stumm, W., and Wersin, P., 1993, A surface complexation model of the carbonate mineral-aqueous solution interface: Geochimica et Cosmochimica Acta, v. 57, n. 15, p. 3505–3518, http://dx.doi.org/10.1016/0016-7037(93)90135-J

Verdoes, D., Kashchiev, D., and van Rosmalen, G. M., 1992, Determination of nucleation and growth rates from induction times in seeded and unseeded precipitation of calcium carbonate: Journal of Crystal Growth, v. 118, n. 3–4, p. 401–413. http://dx.doi.org/10.1016/0022-0248(92)90089-2

Waly, T., Kennedy, M. D., Witkamp, G.-J., Amy, G., and Schippers, J. C., 2012, On the induction time of $CaCO_3$: Effect of ionic strength: Desalination and Water Treatment, v. 39, n. 1–3, p. 55–69. http://dx.doi.org/10.1080/19443994.2012.669159

Westin, K.-J., and Rasmuson, Å.C., 2005, Nucleation of calcium carbonate in presence of citric acid, DTPA, EDTA and pyromellitic acid: Journal of Colloid and Interface Science, v. 282, n. 2, p. 370–379, http://dx.doi.org/10.1016/j.jcis.2004.09.071

White, W. M., 2013, Geochemistry, 1st edition: Hoboken, New Jersey, Wiley-Blackwell, 668 p.

Wikstrom, H., ms, 2007, Understanding hydrate formation in aqueous pharmaceutical environments: Ann Arbor, Michigan, ProQuest Information and Learning Company, Ph. D. thesis, 201 p.

Wu, D. T., 1996. Nucleation theory, *in* Ehrenreich, H., and Spaepen, F., editors, Solid State Physics: Boston, Academic Press, p. 37–187.

Zhang, B., Wu, Q., and Sun, D., 2008, Effect of surfactant Tween on induction time of gas hydrate formation: Journal of China University of Mining and Technology, v. 18, n. 1, p. 18–21, http://dx.doi.org/10.1016/S1006-1266(08)60004-8

Zhao, L., Zhu, C., Ji, J., Chen, J., and Teng, H. H., 2013, Thermodynamic and kinetic effect of organic solvent on the nucleation of nesquehonite: Geochimica et Cosmochimica Acta, v. 106, p. 192–202, http://dx.doi.org/10.1016/j.gca.2012.12.029